ORIGINAL PAPER

Effect of annealing temperatures on the structure and leakage mechanisms of BiFeO$_3$ thin films prepared by the sol–gel method

D. H. Kuang · P. Tang · S. H. Yang · Y. L. Zhang

Abstract In this paper, we report the fabrication of polycrystalline BiFeO$_3$ (BFO) thin films on Pt(111)/Ti/SiO$_2$/Si(100) substrates by the sol–gel method. The effect of annealing temperature (T_a) on the structural, optical, morphological, ferroelectric and leakage properties of the films were analyzed by X-ray diffraction (XRD), Raman spectroscopy, Atomic force microscope (AFM) and ferroelectric measurements. XRD patterns and micro-Raman spectra demonstrated that all films had a single perovskite-type rhombohedral structure. A distortion in crystal lattice constants and a contraction in unit cell volume were observed with the increase of annealing temperatures. AFM images showed that dense and uniform grains were obtained. This reveals that the film is well crystallized. The data of ferroelectric test indicated that the double remanent polarization (2P_r) value of the thin film at $T_a = 600$ °C was 22 μC/cm^2 and the leakage current density was 9.0×10^{-8} A/cm^2 at an applied electric field of 1.0×10^5 V/cm. The leakage mechanisms of thin films have been studied in order to identify the cause of high leakage currents such as Ohmic conduction, the space-charge-limited current, the Schottky emission, the Fowler–Nordheim tunneling and the Poole–Frenkel emission. In low electric field region ($<1.0 \times 10^5$ V/cm), the conduction behavior was found to be dominated by Ohmic conduction for the thin film annealed at 500 °C. The Ohmic conduction and space-charge-limited current dominated the leakage behavior for the thin films at $T_a = 550$ and 600 °C. Fowler–Nordheim tunneling was responsible for the leakage behavior of the thin films at $T_a = 550$, 600 °C in high electric field region ($>1.0 \times 10^5$ V/cm). The results demonstrated that the microstructure, surface morphology and ferroelectric properties of BFO thin films have a strong dependence on annealing temperatures.

1 Introduction

Multiferroic materials combine two or more properties of ferromagnetism, ferroelectricity, and ferroelasticity [1–4]. Because of its potential device applications and fascinating physic essence, such as the information storage, transducer, and magnetoelectric coupling etc. [5, 6], BiFeO$_3$ (BFO) has been extensively studied. Though BiFeO$_3$ is promising, some obstacles, such as large leakage current density and weak ferroelectric properties, still need to be overcome before its applications in multiferroic devices [7]. Especially, the high leakage current density (J) is undesired in the memory devices. Efforts have been made to reduce the leakage current density by either introducing dopants or using different fabrication methods [8–14]. Chung et al. [15] reported that the polycrystalline Mn-doped, Nb-doped, and pure BFO films were fabricated by chemical solution deposition method, in which the Nb dopant is effective in improving electrical properties of BFO films. Yang et al. [16] reported that the nanocomposite (BiFeO$_3$)$_{0.5}$:(Sm$_2$O$_3$)$_{0.5}$ films were deposited on (001) oriented Nb-doped SrTiO$_3$ substrates by PLD, in which the leakage

D. H. Kuang · P. Tang · S. H. Yang · Y. L. Zhang (✉)
State Key Laboratory of Optoelectronic Materials and Technologies, School of Physics and Engineering, Sun Yat-Sen University, Guangzhou 510275, China
e-mail: stszyl@mail.sysu.edu.cn

D. H. Kuang
College of Mathematics and Physics, Xinjiang Agricultural University, Urumqi 830052, China

current density of nanocomposite films was reduced by three orders of magnitude in comparison with the as-deposited pure BFO films.

A few reports have discussed the mechanism of the leakage current of the $BiFeO_3$ film [17]. The leakage mechanism is affected by many factors, such as annealing temperature [18, 19], dopants [12, 20], film thickness [21, 22], and electrodes [16, 23]. Regarding annealing temperatures, Ren et al. [24] reported that the BFO film annealed at 715 °C via sol–gel derived technique exhibited the best dielectric properties with a high dielectric permittivity and a low dielectric loss, however, BFO film had a low remanent polarization value ($P_r \approx 1.3$ μC/cm^2). Chang et al. [25] and Yi et al. [26] reported that the films annealed at 400, 620 °C by pulse laser deposition exhibited the maximum remanent polarization of 60, 108 μC/cm^2, but these thin films had a relatively large leakage current density of 5.0×10^{-4}, 5.5×10^{-5} A/cm^2 at $E = 1.5 \times 10^5$, 2.5×10^5 V/cm, respectively.

Therefore, in the present work, we investigate the effect of annealing temperatures (T_a) on the structural, optical, morphological, ferroelectric and leakage properties of pure BFO thin films fabricated by a sol–gel method and hope to clarify the leakage mechanisms through different annealing temperatures. This study will provide useful information for the fabrication of high quality BFO films and help guide future work to integrate BFO into functional microelectronic devices.

2 Experimental procedure

BFO precursor solutions were prepared using $Fe(NO_3)_3 \cdot 9H_2O$ (98.5 % in purity, Sinopharm Chemical Reagent Co., Ltd) and $Bi(NO_3)_3 \cdot 5H_2O$ (99 % in purity, Sinopharm Chemical Reagent Co., Ltd) as raw materials by a sol–gel process. To compensate Bi loss during the high-temperature process, excess 5 mol% bismuth nitrate pentahydrate was added. Bismuth nitrate and iron nitrate with a mole ratio of 1.05:1 were firstly dissolved in the 2-methoxyethanol, and then a small amount of acetic anhydride was added to the solution to be used as dehydrating agent of the raw materials. The final concentration of the precursor solution was 0.1 mol/L. The solutions were stirred for 3 h and dissolved to form the coating solution at room temperature.

This solution was spread on Pt(111)/Ti/SiO$_2$/Si(100) substrates using spin coating. The thin films depositions were carried out layer by layer using spin coating at 3,000 rpm for 30 s. Each layer was prefired at 350 °C for 10 min in air to decompose remaining organic compounds in the films. This process was repeated for 15 times until the desired thickness ($\sim$320 nm) was obtained. Finally, the

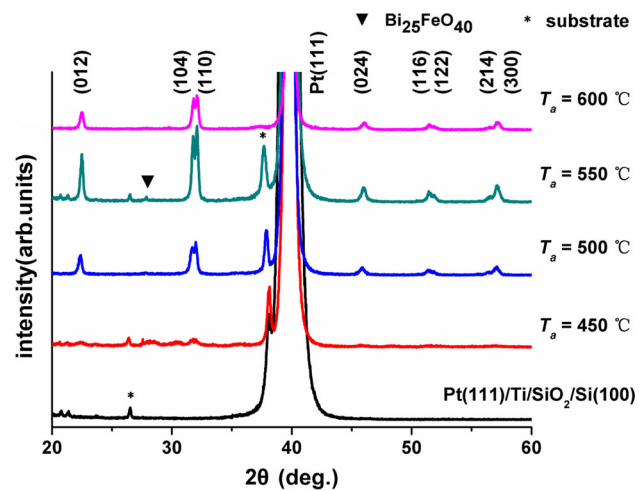**Fig. 1** X-ray diffraction patterns for the pure BFO thin films at various annealing temperatures

thin films were annealed by a rapid thermal process for 15 min in air at $T_a = 450, 500, 550, 600$ °C, respectively. For electrical measurements, top Pt electrodes (diameter $\sim$200 μm) were deposited through a mask on the films by sputtering equipment (JS-1600). The films with top electrodes were annealed at 300 °C for 10 min for the electrode and the film to achieve full contact.

The structure of $BiFeO_3$ thin films was analyzed by an X-ray diffractometer (D-MAX 2200 VPC, RIGAKU) in θ–2θ mode with Cu $K\alpha$ radiation. The scan step length was 0.02°, the scan speed was 1°/min, and the scan range was from 20° to 60°. The Raman spectroscopy of $BiFeO_3$ thin films was analyzed by a Confocal Micro-Raman Spectrometer (inVia Reflex, Renishaw) with 514 nm excitation source under air ambient condition. The microstructure and surface roughness characterization was carried out by using Atomic force microscope (AFM; SPI 3800N, Seiko). The thickness of the thin films was measured by thermal FE Environment scanning electron microscope (SEM; Quanta 400, Dutch Philips). The leakage current density–applied field (J–E) characteristics of the thin films were obtained using a ferroelectric test system (Precision Premier II, Radiant).

3 Results and discussion

Figure 1 shows the X-ray diffraction (XRD) patterns for the pure BFO thin films prepared on Pt(111)/Ti/SiO$_2$/Si(100) substrates heat-treated at different annealing temperatures. The pattern of Pt(111)/Ti/SiO$_2$/Si(100) substrate is also presented for comparison. From the XRD analysis, all the thin film samples are indexed with reference to the perovskite-type rhombohedral structure from 500 to 600 °C with a small amount phase of $Bi_{25}FeO_{40}$, which

Table 1 Structural and micro-structural properties of BiFeO₃ thin films

T_a (°C)	(a) Å	(c) Å	c/a	Cell volume Å³	Crystallite size (nm) from XRD	Grain size (nm) from AFM	Roughness RMS (nm)
500	5.543	13.913	2.510	370.24	49.12	93.89	4.522
550	5.531	13.918	2.516	368.76	66.97	128.9	5.458
600	5.530	13.799	2.495	365.58	45.00	81.68	4.890

Fig. 2 AFM images: **a–c** surface morphology of the BFO thin films annealed at T_a = 500, 550, 600 °C, and **d** the cross-section SEM image of the BFO thin film annealed at T_a = 550 °C
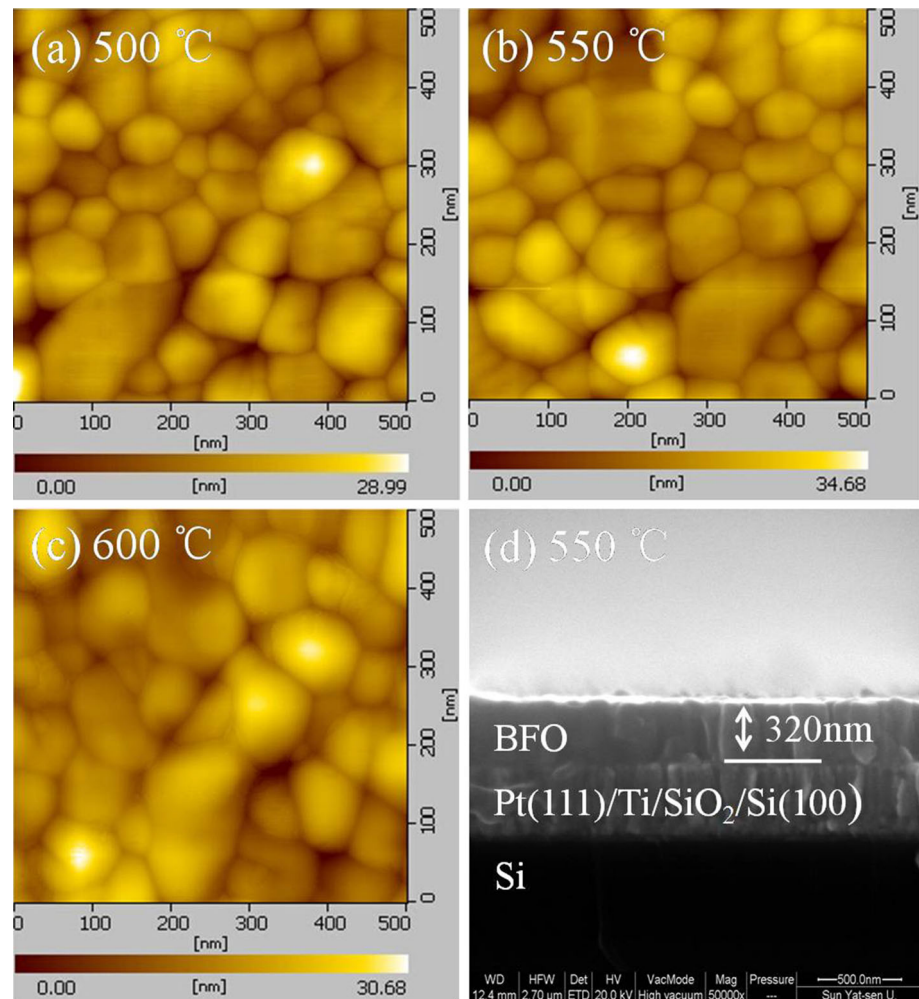
was induced by the Bi-excess in the thin films, in agreement with the results obtained by Yi et al. [26]. However, BFO thin film shows poor crystallization at a lower T_a = 450 °C. From the calculated values of the lattice parameters, c/a ratios and cell volumes reported in Table 1, it was observed that there was a decrease in both "a" and "c" parameters of the unit cell with increasing annealing temperatures leading to unit cell volume contraction. The average crystallite size values reported in Table 1 were determined from the FWHM of the major peak using Scherrer's formula.

Figure 2a–c show the AFM images of surface morphology of BFO thin films annealed at T_a = 500, 550, 600 °C. Dense and uniform morphology and low roughness are obtained for all the thin films from Fig. 2. As evident from Table 1, the average grain sizes of BFO thin films at T_a = 500, 550, 600 °C are approximately 94, 129, 82 nm, respectively. The grain size of the thin film and surface roughness are larger at T_a = 550 °C, which reveal that the film is better crystallized, in agreement with the results of XRD intensity from Fig. 1. Few pores were observed among the grains on the surface. That was because a
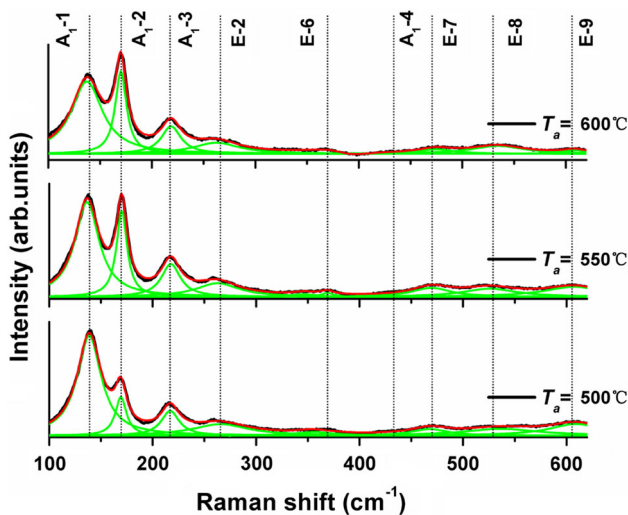
Fig. 3 Raman spectra measured at room temperature for the pure BFO thin films at various annealing temperatures
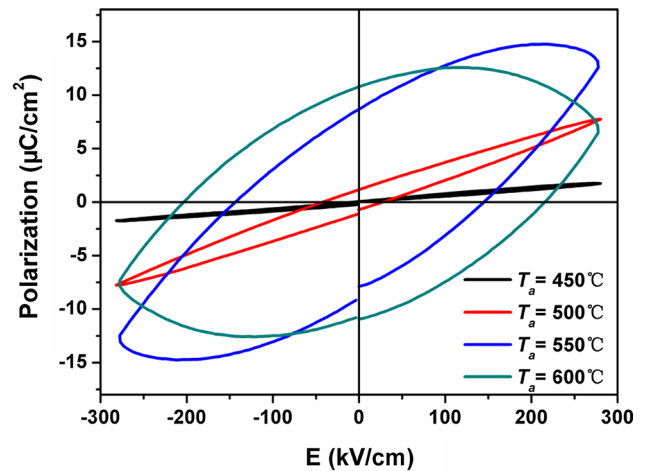

Fig. 4 Ferroelectric hysteresis loops of the BFO thin films measured at 10 kHz

Table 2 Raman shift (in cm^{-1}) obtained for the pure BFO thin films at room temperature

Present results at room temperature			Raman mode	Mao et al. [11] at room temperature	Raghavan et al. [31] at room temperature	Xue et al. [32] at room temperature
$T_a = 500$ °C	$T_a = 550$ °C	$T_a = 600$ °C				
138.7	136.6	137.2	A_1-l	146.4	137	141
169.3	170.1	170.1	A_1-2	166.1	168	172
217.1	217.6	218.6	A_1-3	220.8	216	219
264.7	262.7	262.3	E-2	247.8	257	265
–	–	–	E-3	274.8	279	–
–	–	–	E-4	318.7	309	–
–	346.1	–	E-5	349.8	341	341
387.1	368.7	382.9	E-6	376.8	363	371
431.9	–	428.0	A_1-4	431.0	–	437
468.9	469.5	475.0	E-7	472.1	467	473
537.1	525.6	534.3	E-8	518.9	–	524
609.2	607.5	608.7	E-9	608.9	–	607

reduction of the total grain boundary surface energy promoted the grain boundary motion and the heat treatment induced the diffusion rate increase. These intensified the grain growth and contributed to the formation of pores [27]. As shown in Fig. 2d, the interface is clear without apparent diffusion between the BFO film and the Pt bottom electrode. BFO film is uniform and has good adhesion to the substrate. The grains in the BFO films deposited on Pt(111)/Ti/SiO$_2$/Si(100) are columnar in the film-growth process. The thickness of the film is approximately 320 nm.

Figure 3 shows the Raman scattering spectra measured at room temperature for the pure BFO thin films. All Raman spectra of these samples have been fitted by Lorentzian components. For the rhombohedral (R3c) BFO, 13 (4A$_1$ + 9E) active Raman modes are predicted by Group theory [28, 29]. It is clear that most of the A$_1$ and E-symmetry normal modes for all the samples can be clearly seen, which are well correlated with those of the rhombohedral perovskite structure. The relative intensity ratios of these low-frequency A$_1$-1 and A$_1$-2 modes decrease with increasing annealing temperatures. The drastic change of the intensities of A$_1$-1 and A$_1$-2 modes, slight broadening and shifting of some A$_1$ and E modes may be related to the change of the Bi–O and Fe–O covalent bonds and the lattice distortion [30]. The results obtained by the Raman scattering spectra analysis for the BFO thin films are listed in Table 2. This table shows a
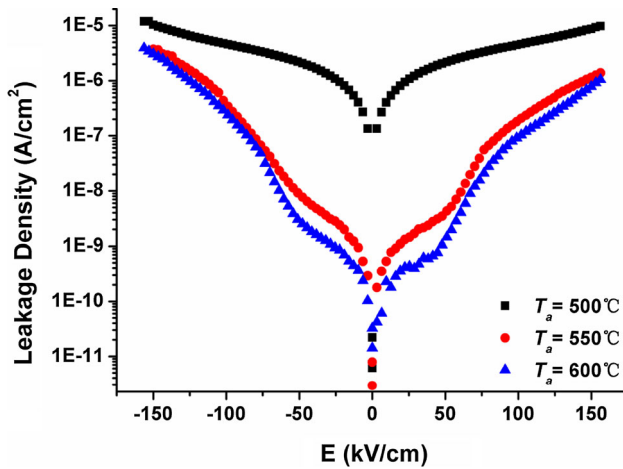
Fig. 5 The leakage current density–applied electric field (J–E) behavior measured at room temperature for the BFO films

comparison in the exact peaks of the Raman active modes for the BFO thin films obtained in this work with those reported in the literatures [11, 31, 32].

The polarization–electric field hysteresis loops measured under the electric field of 2.8×10^5 V/cm at room temperature for the BFO thin films with different T_a are presented in Fig. 4. The double remanent polarization of BFO films increases with the increase of T_a. The double remanent polarizations of BFO films are 0.08, 2.3, 17.7, 22 $\mu C/cm^2$ for the BFO film at $T_a = 450$, 500, 550, 600 °C, respectively. For the BFO film at $T_a = 450$ °C, it is unable to get a well hysteresis loop due to its large leakage current. The remanent polarizations at $T_a = 550$, 600 °C are larger than those of the sol–gel films reported in the references [7, 24, 33].

Figure 5 shows the leakage current density versus applied electric field (J–E) characteristics of the BFO thin films at $T_a = 500$, 550, 600 °C. The J–E characteristics of all the films at negative and positive biases are symmetric. The leakage current density of each film increases as the electric field is increased. At a given electric field, the leakage current density decreases with T_a increase, which is consistent with the results reported in the literature [25]. The value of the leakage current density for the thin film of $T_a = 600$ °C is 9×10^{-8} A/cm^2 under 1.0×10^5 V/cm,
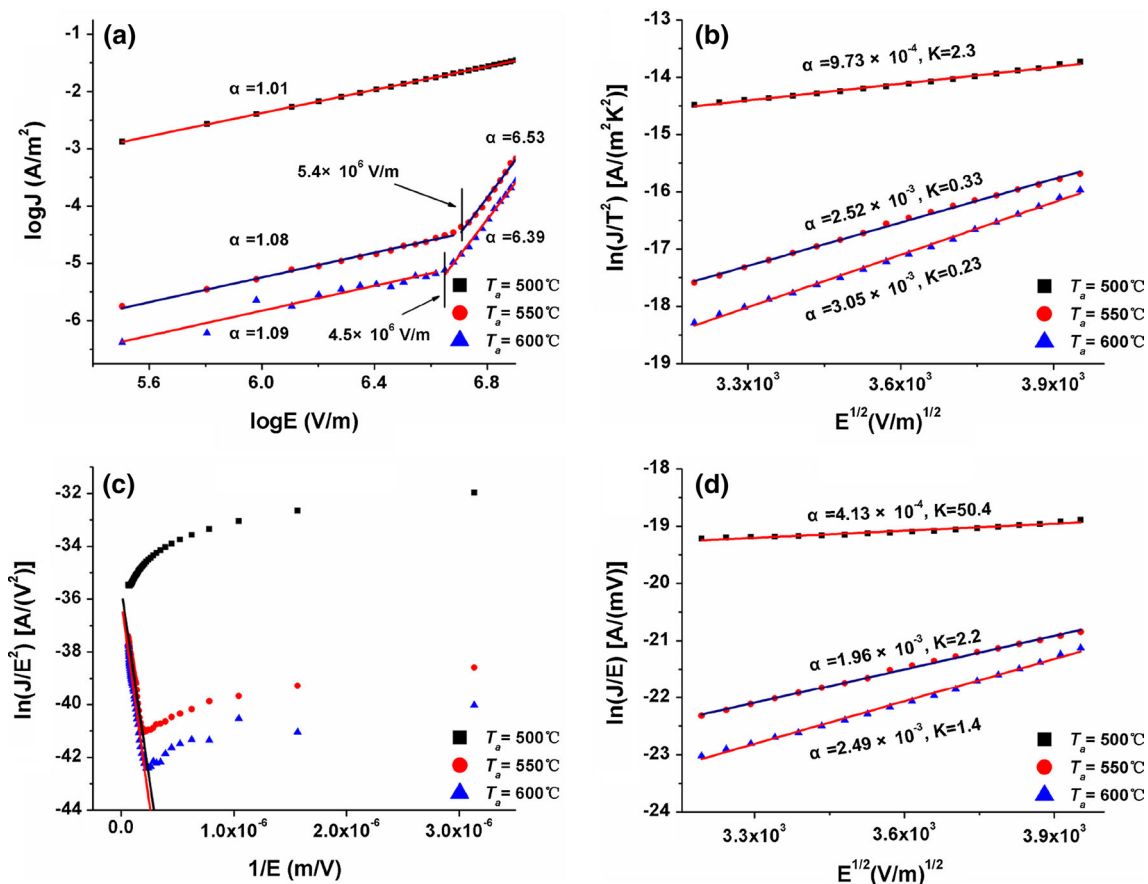

Fig. 6 The leakage current density versus electric field characteristics of the BFO thin films measured at room temperature. **a** Ohmic conduction and SCLC, **b** SE, **c** FN tunneling and **d** PF emission

which is reduced by two orders of magnitude compared to that of the BFO film of $T_a = 500$ °C. This can be attributed to the uniform surface morphology and less pinholes for the thin film of $T_a = 600$ °C.

Different leakage mechanisms have been widely used to investigate the J-E characteristics of BFO thin films: the Schottky emission (SE), the Fowler–Nordheim (FN) tunneling, the space-charge-limited current (SCLC) and the Poole–Frenkel (PF) emission [5, 9, 13, 18, 34]. The SE and FN tunneling are interface-limited conduction, whereas the SCLC and PF emission are bulk-limited conduction. Figure 6a shows $\log J$–$\log E$ curves of a positive bias at $T_a = 500$, 550 and 600 °C. The $\log J$–$\log E$ behavior shows linear characteristics with different slopes for different T_a at low electric fields. The slopes for the films at $T_a = 500$, 550 and 600 °C are 1.01, 1.08 and 1.09, respectively. These values are close to one and the conduction behaviors show Ohmic conduction, which can be expressed by [35]

$$J = en\mu E, \tag{1}$$

where e is the electronic charge, n is the number of charge carriers, and μ is the carrier mobility. The slope values for the BFO films at $T_a = 550$, 600 °C are 6.53 and 6.39 after the electric fields above 5.4×10^6, 4.5×10^6 V/m, respectively. These values are much larger than one. Such a leakage behavior indicates a power law relationship $J \propto E^n$ ($n > 1$), which is a characteristic of space-charge-limited conduction (SCLC) [1, 32]. The abrupt increase in the leakage current may be originated from all the available traps becoming filled by the applied voltage, and can be well explained by the trap-filled-limit (TFL) law [36].

The interface limited Schottky emission arises from the Schottky barrier at the interface of the metal electrode and dielectric [17, 34] and is described by

$$J = A^* T^2 \exp\left[\frac{-\left(\phi_B - e\sqrt{eE/4\pi\varepsilon_0 K}\right)}{k_B T}\right], \tag{2}$$

$$K = \frac{e^3}{k_B^2 T^2 \times 4\pi\varepsilon_0 \alpha^2}, \tag{3}$$

where A^* is Richardson constant, ϕ_B is Schottky barrier height and K is optical dielectric constant.

Figure 6b shows $\ln(J/T^2)$–$E^{1/2}$ curves of a positive bias at $T_a = 500$, 550 and 600 °C. As shown in Fig. 6b, linear fittings are obtained at high electric fields (between 1×10^7 and 1.6×10^7 V/m). If the leakage current is governed by SE, a linear relation between $\ln(J/T^2)$ and $E^{1/2}$ with a slope of $e\sqrt{e/4\pi\varepsilon_0 K}/k_B T$ should be obtained. According to the linear fittings in Fig. 6b, the K value can be derived by the Eq. (3). The refraction index for BFO is known to be $n = 2.5$, and thus an optical dielectric permittivity of $K = n^2 = 6.25$ is expected [37]. The K values

for the BFO films at $T_a = 500$, 550, 600 °C are 2.3, 0.33 and 0.23, respectively. These values are much less 6.25. This suggests that there is no Schottky effect in the BFO thin film.

The injection of charge carriers into an insulator layer from electrodes may take place by tunneling through an interfacial energy barrier. This effect is called FN tunneling and can be expressed by [23, 34]

$$J = BE^2 \exp\left(\frac{-C\phi_i^{3/2}}{E}\right), \tag{4}$$

where B and C are constants and ϕ_i is the potential barrier height. Figure 6c shows $\ln(J/E^2)$ versus $(1/E)$ curves at positive bias. As shown in Fig. 6c, a linear relation between $\ln(J/E^2)$ and $(1/E)$ with negative slope for the BFO thin films at $T_a = 550$, 600 °C can be observed in the high electric field region. That is to say, the leakage mechanism is dominated by the FN mechanism for the BFO thin films at $T_a = 550$, 600 °C. The FN mechanism indicates the formation of a partial depletion layer between the thin film and the electrode. The FN mechanism also indicates that the potential barrier height of interfacial layer decreases with increasing annealing temperature.

The PF emission mechanism originates from the field-assisted thermal ionization of trapped carriers into the conduction band of thin films. The leakage current density controlled by the PF emission can be expressed as [17]

$$J = AE \exp\left[\frac{-\left(\Phi_t - e\sqrt{eE/\pi\varepsilon_0 K}\right)}{k_B T}\right], \tag{5}$$

$$K = \frac{e^3}{k_B^2 T^2 \times \pi\varepsilon_0 \alpha^2}, \tag{6}$$

where A is a constant, ϕ_t is the trap ionization energy, ε_0 is the permittivity of free space, K is the optical dielectric constant, k_B is the Boltzmann constant and T is the temperature, and α is the linear fitting slope. Figure 6d shows the $\ln(J/E)$ versus $E^{1/2}$ plots of the BFO films at high electric fields (between 1×10^7 and 1.6×10^7 V/m). If the leakage current is governed by PF emission, a linear relation between $\ln(J/E)$ versus $E^{1/2}$ with a slope of $e\sqrt{e/\pi\varepsilon_0 K}/k_B T$ should be obtained. According to the slope from the linear fittings in Fig. 6d, the K values derived by the Eq. (6) for the BFO films at $T_a = 500$, 550, 600 °C are 50.4, 2.2 and 1.4, respectively. The results show the optical dielectric constants of all the BFO films were not close to 6.25. That is to say, the PF emission does not exist in the BFO films.

In summary, the leakage current density in BFO thin film prepared by a simple sol–gel spin-coating method is found to be subject to Ohmic conduction at $T_a = 500$ °C

for the low electric field. The serious transient effect from the traps is observed in BFO thin films at $T_a = 550, 600$ °C and the leakage current densities are subject to Ohmic conduction and SCLC. The leakage mechanism is dominated by the FN instead of SE or PF mechanism for the BFO thin films at $T_a = 550, 600$ °C for the high electric field.

4 Conclusions

In summary, BFO films were successfully prepared on Pt(111)/Ti/SiO$_2$/Si(100) substrates by the sol–gel method. The effect of T_a on the structure and electrical properties of BFO films was investigated. XRD patterns revealed that all the films have a pure phase related to perovskite-type rhombohedral structure from 500 to 600 °C. The results of Rietveld refinement showed that a distortion in crystal lattice constants and contraction in unit cell volume was observed with the increase of annealing temperatures. AFM and SEM images showed that the crystallization of thin films were very good and dense, and uniform grains were obtained. The grains in the BFO films deposited on Pt(111)/Ti/SiO$_2$/Si(100) were columnar. The data of ferroelectric test indicated that the value of $2P_r$ was 22 μC/cm^2 and the leakage current density was 9×10^{-8} A/cm^2 at an applied electric field of 1.0×10^5 V/cm for the BFO film at $T_a = 600$ °C due to the uniform grains, smooth surface and the low leakage current density. The leakage current mechanism of the BFO films could be considered as follows: the leakage behavior was found to be dominated by Ohmic and space-charge-limited conduction for all the BFO thin films in low electric field region. Fowler–Nordheim tunneling was responsible for the leakage behavior of the thin films for $T_a = 550, 600$ °C in high electric field region. The results show that the microstructure, surface morphology and ferroelectric properties of BFO thin films had a strong dependence on T_a.

References

1. Qi XD, Dho J, Tomov R, Blamire MG, MacManus-Driscoll JL (2005) Appl Phys Lett 86:062903
2. Velasco-Davalos IV, Moretti M, Nicklaus M, Nauenheim C, Li S, Nechache R, Gomez-Yanez C, Ruediger A (2014) Appl Phys A 115:1081–1085
3. Li YT, Fan YW, Zhang HG, Teng XX, Dong XG, Liu H, Ge XP, Li Q, Chen W, Li XA, Ge ZY (2014) J Supercond Nov Magn 27:1239–1243
4. Muneeswaran M, Jegatheesan P, Gopiraman M, Kim IS, Giridharan NV (2014) Appl Phys A 114:853–859
5. Zhong ZY, Ishiwara H (2009) Appl Phys Lett 95:112902
6. Michel C, Moreau JM, Achenbach GD, Gerson R, James WJ (1969) Solid State Commun 7:701
7. Wang Y, Nan CW (2006) Appl Phys Lett 89:052903
8. Raghavan CM, Kim JW, Kim SS (2013) J Sol–Gel Sci Technol 67:486–491
9. Naganuma H, Okamura S (2007) J Appl Phys 101:09M103
10. Kim YJ, Kim JW, Kim SS (2013) J Sol–Gel Sci Technol 66:38–42
11. Mao WW, Wang XF, Han YM, Li XA, Li YT, Wang YF, Ma YW, Feng XM, Yang T, Yang JP, Huang W (2014) J Alloy Compd 584:520–523
12. Li DH, Sun XQ, Chuai XH, Wu ZF, Cao ZJ, Yan YF, Zhang DM (2012) J Cryst Growth 338:85–90
13. Shuai Y, Ou X, Wu CG, Zhang WL, Zhou SQ, Bürger D, Reuther H, Slesazeck S, Mikolajick T, Helm M, Schmidt H (2012) J Appl Phys 111:07D906
14. Simões AZ, Cavalcante LS, Riccardi CS, Varela JA, Longo E (2007) J Sol–Gel Sci Technol 44:269–273
15. Chung CF, Lin JP, Wu JM (2006) Appl Phys Lett 88:242909
16. Yang H, Wang H, Zou GF, Jain M, Suvorova NA, Feldmann DM, Dowden PC, DePaula RF, MacManus-Driscoll JL, Taylor AJ, Jia QX (2008) Appl Phys Lett 93:142904
17. Simões AZ, Cavalcante LS, Moura F, Longo E, Varela JA (2011) J Alloy Compd 509:5326–5335
18. Yan F, Lai M-O, Lu L, Zhu T-J (2011) J Phys D Appl Phys 44:435302
19. Yang H, Jain M, Suvorova NA, Zhou H, Luo HM, Feldmann DM, Dowden PC, DePaula RF, Foltyn SR, Jia QX (2007) Appl Phys Lett 91:072911
20. Xue X, Tan GQ (2013) J Alloy Compd 575:90–95
21. Tang XW, Dai JM, Zhu XB, Yin LH, Ang R, Song WH, Yang ZR, Sun YP (2010) J Am Ceram Soc 93(6):1682–1687
22. Tang XW, Dai JM, Zhu XB, Lin JC, Chang Q, Wu DJ, Song WH, Sun YP (2012) J Am Ceram Soc 95(2):538–544
23. Pabst GW, Martin LW, Chu Y-H, Ramesh R (2007) Appl Phys Lett 90:072902
24. Ren YJ, Zhu XH, Zhang CY, Zhu JL, Zhu JG, Xiao DQ (2014) Ceram Int 40:2489–2493
25. Chang HW, Yuan FT, Tien SH, Shen CY, Wang CR, Jen SU (2014) IEEE Trans Magn 50(1):2500604
26. Yi ML, Wang BC, Shen Q, Zhang LM (2014) J Mater Sci: Mater Electron 25:82–86
27. Cavalcante LS, Sczancoski JC, De Vicente FS, Frabbro MT, Siu Li M, Varela JA, Longo E (2009) J Sol–Gel Sci Technol 49:35–46
28. Singh MK, Jang HM, Ryu S, Jo MH (2006) Appl Phys Lett 88:042907
29. Rout D, Moon KS, Kang SJL (2009) J Raman Spectrosc 40:618–626
30. Singh MK, Ryu S, Jang HM (2005) Phys Rev B 72:132101
31. Raghavan CM, Kim JW, Kim SS (2014) Ceram Int 40:2281–2286
32. Xue X, Tan GQ, Hao HF, Ren HJ (2013) Appl Surf Sci 282:432–438
33. Shannigrahi SR, Huang A, Chandrasekhar N (2007) Appl Phys Lett 90:022901
34. Chen ZH, He L, Zhang F, Jiang J, Meng JW, Zhao BY, Jiang AQ (2013) J Appl Phys 113:184106
35. Chaudhuri AR, Krupanidhi SB (2008) J Appl Phys 104:104102
36. Yang KG, Zhang YL, Yang SH, Wang B (2010) J Appl Phys 107:124109
37. Iakovlev S, Solterbeck CH, Kuhnke M, Es-Souni M (2005) J Appl Phys 97:094901